SAND2023-12251J

Graphical Abstract

Electrochemically induced fracture in LLZO: How the interplay between flaw density and electrostatic potential affects operability

Scott Monismith, Jianmin Qu, Rémi Dingreville

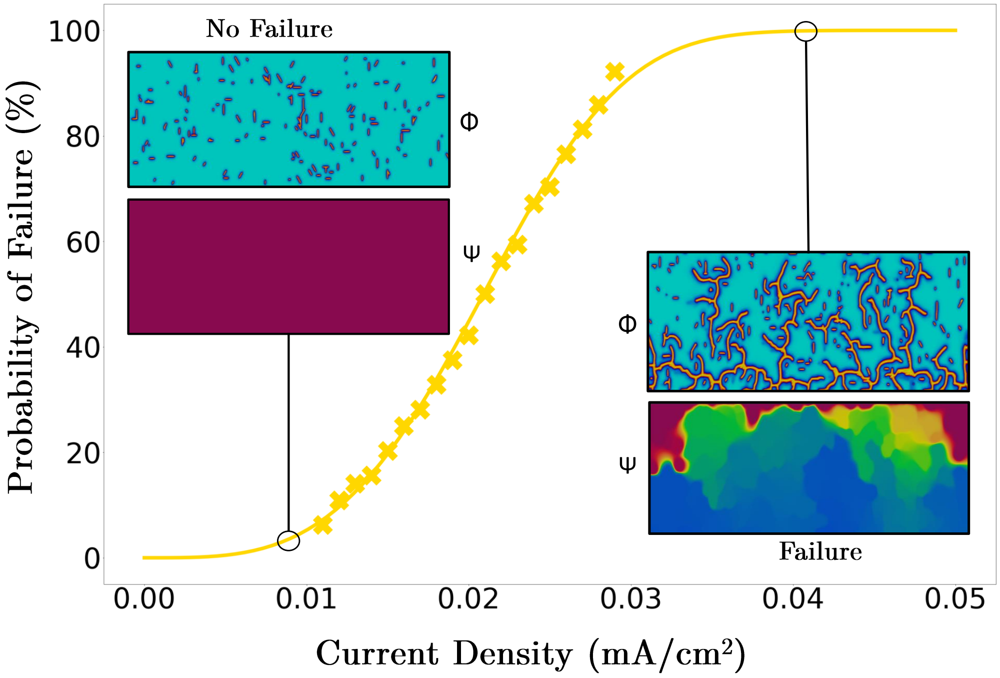

This article has been authored by an employee of National Technology & Engineering Solutions of Sandia, LLC under Contract No. DE-NA0003525 with the U.S. Department of Energy (DOE). The employee owns all right, title and interest in and to the article and is solely responsible for its contents. The United States Government retains and the publisher, by accepting the article for publication, acknowledges that the United States Government retains a non-exclusive, paid-up, irrevocable, world-wide license to publish or reproduce the published form of this article or allow others to do so, for United States Government purposes. The DOE will provide public access to these results of federally sponsored research in accordance with the DOE Public Access Plan https://www.energy.gov/downloads/doe-public-access-plan.

Electrochemically induced fracture in LLZO: How the interplay between flaw density and electrostatic potential affects operability

Scott Monismith[a,*], Jianmin Qu[a,b], Rémi Dingreville[c]

[a] *Tufts University, Medford, MA 02155, USA*
[b] *Stevens Institute of Technology, Hoboken, NJ 07030, USA*
[c] *Center for Integrated Nanotechnologies, Nanostructure Physics Department, Sandia National Laboratories, Albuquerque, NM 87185, USA*

Abstract

Fracture and short circuit in the $Li_7La_3Zr_2O_{12}$ (LLZO) solid electrolyte are two key issues that prevent its adoption in battery cells. In this paper, we utilize phase-field simulations that couple electrochemistry and fracture to evaluate the maximum electric potential that LLZO electrolytes can support as a function of crack density. In the case of a single crack, we find that the applied potential at the onset of crack propagation exhibits inverse square root scaling with respect to crack length, analogous to classical fracture mechanics. We further find that the short-circuit potential scales linearly with crack length. In the realistic case where the solid electrolyte contains multiple cracks, we reveal that failure fits the Weibull model. The failure distributions shift to favor failure at lower overpotentials as areal crack density increases. Furthermore, when flawless interfacial buffers are placed between the applied potential and the bulk of the electrolyte, failure is mitigated. When constant currents are applied, current focuses in near-surface flaws, leading to crack propagation and short circuit. We find that buffered samples sustain larger currents without reaching unstable overpotentials and without failing. Our findings suggest several mitigation strategies for improving the ability of LLZO to support larger currents and improve operability.

Keywords: Solid electrolyte, LLZO, Fracture, Phase-field simulation

---

[*] Corresponding author

Email address: `scott.monismith@tufts.edu` (Scott Monismith)

Preprint submitted to Journal of Power Sources *February 9, 2023*

1. Introduction

As the demand for sustainable energy and energy storage grows, there is an urgent need by the industry to replace Li-ion liquid-state electrolytes by Li-ion solid-state batteries as a safe, non-flammable, and resilient alternative solution. Among the various solid-state electrolytes solutions, garnet-type Li-ion electrolytes based on cubic $Li_7La_3Zr_2O_{12}$ (LLZO) are considered promising candidates for the realization of safe and stable Li metal batteries. Indeed, not only do LLZO solid electrolytes possess a high ionic conductivity (10^{-4} scm^{-1}) and stability with respect to Li metal [1, 2], but owing to large shear modulus, they can also inhibit the nucleation and growth of Li metal dendrites via mechanical suppression [3–7].

However, these electrolytes are susceptible to penetration by a network of Li metal filaments [8–11], resulting in short circuit. One proposed mechanism for this short circuit is that local inhomogeneities in Li plating on the anode surface lead to large local stresses, causing fracture in LLZO, and subsequently creating more topological diversity aggravating the propensity for inhomogeneous Li deposition. Indeed, many research groups have reported crack propagation under fairly low electrochemical loads, with concomitant Li metal filament deposition along the crack pathways [9, 12, 13]. This short-circuit mechanism is clearly heavily dependent on the flaw-tolerance of LLZO. Experimental and modeling studies have shown that LLZO has a fracture toughness of roughly 1 $\mathrm{MPa}.\sqrt{\mathrm{m}}$ [7, 14–16]. From this comparatively low toughness, it is reasonable to posit that the failure of LLZO will be driven predominantly by Griffith cracks inevitably present in the material's microstructure. Studies such as those listed above reveal that failure of LLZO-based cells encapsulates a nuanced interplay between local electrochemical phenomena and mechanical fracture processes.

Solutions are currently being explored to solve the issues exposed above. The simplest cell architectural change that could improve the operability of LLZO would be to electrically shield the electrolyte via an insulating membrane, such as a polypropylene separator. However, this membrane needs to be capable of conducting Li^+ ions; to that end, a membrane wetted with traditional liquid electrolyte would meet these criteria and facilitate an even distribution of current. Several research groups in academia and industry have found success combining liquid electrolytes with LLZO [17, 18]. This strategy is self-defeating insofar as a key impetus for using solid electrolytes is eliminating the highly volatile liquid electrolytes. One recent study demonstrated that solid-state cells with added liquid do not necessarily offer a significant safety improvement over conventional cells [19]. An alternative architectural change would be to apply external pressure to the cell to reduce interfacial impedance and help distribute the current evenly. Furthermore, this applied pressure opposes the tensile driving force for crack propagation, effectively toughening the material. While this is an appealing strategy, the effect of this external pressure is mixed; some reports indicate that the external pressure can neither be too high nor too low for it to be an effective strategy [20–22]. If the pressure is too low, the interfacial impedance remains high, while excessive pressures will lead to tensile reaction stresses which can cause crack propagation. Moreover, adding a pressurizing mechanism to a battery pack adds cost and difficulty.

Perhaps a better mechanism for interfacial toughening is that proposed by Qi et al. [10]. They suggest that imparting residual compressive stresses in the material via ion exchange or ion implantation improves the cycling characteristics of LLZO at the cost of a small decrease in conductivity. This strategy is attractive in that it requires no additional cell or pack components to function. Additionally, compressive stresses may be able to heal near-surface cracks, decreasing the local electrical conductivity, and shielding the bulk from the effects of the electric field. Thus, such microstructural treatment addresses the dendrite problem from both a mechanical and electrical perspective, increasing the likelihood of success. One outstanding question regarding this approach though is how do these flaws (microcracks, defect clusters) imparted by ion implantation affect the overall operability of the electrolyte?

Researchers have conducted molecular dynamics and finite element studies to better understand the fracture behavior in LLZO. For instance, in our prior work [16] we simulated grain-boundary fracture using atomistic simulations and found that fracture in LLZO is associated with a clustering of Li ions in the vicinity of the growing crack, indicating an alteration of local transport properties. Similarly, Yu and Siegel [23] proposed that the relative softness of grain-boundaries leads to preferential deposition of lithium along these boundaries, causing fracture. This mechanism was further elucidated by Barai et al. [15, 24] in their finite element simulations, showing that the strain energy density in LLZO is greatest at the grain boundaries due to current focusing of Li ions. However, these techniques cannot precisely account for the growth of a Li metal deposit and the associated Li-LLZO interface.

These limitations motivate the development of mesoscale models which can describe the growth of interfaces (lithium-electrolyte or cracked-uncracked interfaces). Phase-field models provide such capabilities and can thoroughly elucidate the topology of growing lithium metal filaments by approximating the concomitant phases as continuous variables. One of the earlier phase-field models in this area showed how the growth of Li metal filaments in a liquid electrolyte is influenced by the applied overpotential as well as by the initial shape of elliptical deposits on the anode surface [25]. This work was able to achieve qualitative results which closely matched the morphology of Li metal filaments observed in experimental studies. Yurkiv et al. [26] extended this model to the solid electrolyte interphase and included the effects of elasticity, showing how the mechanical stresses and strains drive growth of filaments. Large hydrostatic stresses at the root of dendrites were hypothesized to be key contributors to their growth. A later result, including Li metal's considerable anisotropy [27, 28], further clarified the role of this hydrostatic stress on Li filament growth. The growth of filaments was also found to be dependent on the local temperature gradients [29] and the concentration gradients within the electrolyte [30].

These models for liquid electrolytes form the basis of many models focusing on solid electrolytes. Indeed, solid electrolyte models use much of the same core physics but with a greater emphasis on the mechanical constraint of the electrolyte as well as the propagation of cracks. Thus, Ren et al. [31] demonstrated that a composite electrolyte comprised of polyethylene oxide and alumina nanofibers could inhibit the growth of dendrites via mechanical suppression, in-line with the results of Monroe and Newman [3]. Along the same lines, a later study on LLZO by Tian and coworkers [32, 33] showed that the high electron affinity of crack surfaces led to preferential deposition along flaws. Similarly, Yuan et al. [20, 34], based on this higher electrical conductivity along cracks, modeled the growth of cracks through LLZO both with and without Li metal. Critically, they found that higher currents and lower toughness led to more rapid short circuit and developed estimates for "safe" operation for single cycles of LLZO-based cells.

To expand on these models, we consider a fracture-mechanics study built upon the thermodynamically consistent frameworks proposed by Miehe et al. [35] and Ambati et al. [36]. Critically, these fracture models have been demonstrated to accurately simulate both mode I and mode II fracture in a variety of load configurations which are considered industry standard. While there are many energy-functional-based phase-field fracture models, these models are some of the most well-validated and they preclude the advance of cracks through regions of compressive stress. This key feature is important, as the stress state during electrochemical loads is complex, with both compressive and tensile components [20, 37]. We are particularly interested in failure mechanisms of LLZO cells which include multiple randomly distributed Griffith cracks; we add this layer of complexity to address the question: "Why do some cells fail while others succeed, despite seemingly identical processing and handling?" To wit, we develop a coupled electrostatics-mechanics model with a thermodynamically rigorous treatment of fracture to probe the onset potentials and critical current densities for failure in LLZO. We leverage this model to generate both deterministic estimates of critical potentials from a largest flaw theory of failure, as well as probabilistic spreads of outcomes given a pseudo-random distribution of cracks. Additionally, we consider the presence of a "buffer" region of flawless crystal between the bulk of the LLZO and the Li metal anode to demonstrate a potential strategy to improve LLZO's resilience to fracture and short circuit.

2. Methods

Our modeling framework is comprised of three components:

1. an electrostatics module which acts as a source term for the subsequent evolution of mechanical stresses and cracks,
2. a mechanical module, which computes the displacement, strain, and stress fields from the applied electric field, and
3. a fracture module, which generates and evolves a crack field from the (tensile) electrochemomechanical source term.

The simulation workflow begins by initiating a crack field from an initial seed of tensile strain energy density. An electric field is then generated from boundary conditions with either a constant voltage or a constant current. From the applied potential, we solve for the mechanical equilibrium equations to find the elastic fields, which drive the growth of cracks. The model then progresses to the next step, where the electric field boundary conditions are modified, and the other fields are updated. This procedure repeats until a prescribed number of steps is completed. We build on the existing phase-field literature in this space while making several key additions and changes. Notably, this model does not explicitly model the development of Li metal filaments. Instead we implicitly assume that lithium metal preferentially deposits through cracks, leading to the development of stresses[9, 20, 32]. While this model does not provide information on the internal state of the Li metal (topology, segregation, *etc.*) that would develop under these conditions, the electric field is sufficient to infer the stress state and crack geometry within the LLZO film. A glossary of symbol and notation is provided in Appendix A.

2.1. Electrostatics

To compute the driving force for crack propagation, the value of the overpotential must be known at each point in the simulation domain. To that end, the current continuity Poisson's equation

$$\nabla \cdot (\sigma^{\mathrm{elec}} \nabla \Psi) = 0, \tag{1}$$

from Chen et al. [25] is solved at each time step to determine the electric field, Ψ, from the applied voltage, V_{applied}. The electrical conductivity, σ^{elec}, is constructed from:

$$\sigma^{\mathrm{elec}} = \mathrm{h}\sigma^{\Phi} + (1 - \mathrm{h})\sigma^{\mathrm{LLZO}}, \tag{2}$$

where σ^{Φ} and σ^{LLZO} are the electrical conductivities of cracked and pristine (uncracked) LLZO respectively, and h represents a switching function which estimates the conductivity in the crack and pristine domains. The specific polynomial is selected to achieve the following conditions: $\mathrm{h}(0) = 0$, $\mathrm{h}(1) = 1$, $\mathrm{h}(\frac{1}{2}) = \frac{1}{2}$, $\mathrm{h}'(0) = \mathrm{h}'(1) = 0$. To that end, we used the polynomial, $\mathrm{h}(\Phi) = \Phi^2(10\text{-}15\Phi + 6\Phi^2)$, where Φ is the phase-field crack variable.

Once the Poisson's equation Eq. (1) is solved, the overpotential must be computed at each point in the domain to determine the stresses. The overpotential, η, can be thought of as the electrical driving force for an electrochemical reaction. It represents a deviation from the electrochemical equilibrium which drives the migration of charged species to restore that equilibrium. Expressing this mathematically:

$$\eta = \Psi - \Psi^{(0)}, \tag{3}$$

characterizes the overpotential in terms of the electric field, Ψ, and the equilibrium potential of the electrochemical reaction at standard temperature and pressure, $\Psi^{(0)}$. As this work will only consider conditions at the interface of

Li-metal and LLZO, a convenient choice of $\Psi^{(0)}$ is the Li/Li$^+$ equilibrium potential. This ensures that if one side of the domain is grounded (Ψ=0), the applied voltage bias on the other side of the domain is equivalent to the applied overpotential. By convention, in this context, a negative voltage bias represents a positive overpotential. For example, a simulation cell grounded on one side with an applied potential of −5 mV on the opposite side would have an applied overpotential of 5 mV.

We simulated two distinct types of electrochemical conditions which differ in the character of the boundary conditions (BC) applied to Eq. (1):

BC 1: $\Psi|_{\mathrm{y=L_y}} = 0$, $\Psi|_{\mathrm{y=0}} = \mathrm{A} \times t$: The potential on the bottom of the simulation cell increases linearly as a function of time at a prescribed rate, A, in mV/sec. The potential on the top of the simulation cell is 0 V.

BC 2: $\sigma^{\mathrm{elec}} \nabla \Psi \cdot \hat{n} = \mathrm{j_{applied}}$,: The current density vector component normal to the bottom surface of the simulation cell is set to a prescribed constant value.

These two types of boundary conditions are analogues of simple laboratory electrochemical experiments; indeed, BC 1 is intended to represent linear sweep voltammetry (LSV), while BC 2 represents an applied constant current.

2.2. Elasticity Model

Once the overpotential is computed at each point in the simulation cell, the mechanical stresses and strains can be calculated to determine the available driving force for crack propagation. The initiation and growth of cracks is based on concentrated strain energy density. Consequently, the distribution of internal forces within the material is found via the mechanical equilibrium equations:

$$\nabla \cdot \left(\boldsymbol{\sigma^0} + \boldsymbol{\sigma^\eta} \right) = 0, \tag{4}$$

where $\boldsymbol{\sigma^\eta}$ represents the stress induced by the local overpotential, η, and $\boldsymbol{\sigma^0}$ is the stress that arises to balance these electrochemical forces. The overpotential-induced stress components are calculated as [9, 20, 34]:

$$\sigma_{ij}^{\eta} = \frac{F\eta}{\Omega_{\mathrm{Li}}} \delta_{ij}, \tag{5}$$

where Ω_{Li} is the partial molar volume of Li, and δ_{ij} is the Kronecker delta tensor. Physically, this quantity represents the stress that Li plating exerts on the inside of a burgeoning crack tip.

These equations must be modified to account for the presence of cracks. Consequently, the stress tensor must include a constitutive relationship that scales the stresses by the phase-field variable, Φ [35, 36]:

$$\boldsymbol{\sigma} = f(\Phi)\mathbb{C} : \boldsymbol{\epsilon}, \tag{6}$$

where Φ represents the phase-field crack variable; $\Phi = 1$ corresponds to entirely broken material, while $\Phi = 0$ corresponds to pristine material. The term, $\mathbb{C} : \boldsymbol{\epsilon}$ represents the classical Cauchy stress. The function f is selected to be $f(\Phi) = (1-\Phi)^2 + k$, and it satisfies the following criteria:

1. $f(0) = 1$, the far-field stresses are equal to the Cauchy stresses.
2. $f(1) = 0$, the stresses in the crack body are zero.
3. $f'(1) = 0$, the fracture energy for a fully broken state must converge to a finite value.

The constant, k, is an arbitrarily small number, included to ensure numerical stability. To solve for the total stress, Eq. (6) is substituted into Eq. (4), scaling both portions of the stress tensor, and the constitutive relations (with Lamé constants μ_{LLZO} and λ_{LLZO}) for this material are applied alongside the strain compatibility equations:

$$\boldsymbol{\sigma} = 2\mu_{\mathrm{LLZO}}\boldsymbol{\epsilon} + \lambda_{\mathrm{LLZO}}\mathrm{tr}(\boldsymbol{\epsilon})\mathrm{I}, \tag{7}$$

$$\epsilon_{ij} = \frac{1}{2}\left(\frac{\partial u_i}{\partial x_j} + \frac{\partial u_j}{\partial x_i}\right). \tag{8}$$

By substituting Eq. (8) into Eq. (7) and then into Eq. (4) we arrive at a set of equations which can be solved for the displacement field associated with the electrochemical loading applied to the sample.

2.3. Phase-Field Crack Model

Once the displacement fields are known, the total strains and associated strain energy densities can be calculated. However, it is critical to note that , at the micro-scale, cracks may only form where the dominant strain is tensile rather than compressive. To that end, we employ the spectral decomposition scheme of Miehe et al. [35] to generate the compressive and tensile portions of the strain tensor:

$$\boldsymbol{\epsilon}_+ := \Sigma_i^\delta \langle \epsilon^i \rangle_+ \left(n^i \otimes n^i \right) \quad \text{and} \quad \boldsymbol{\epsilon}_- := \Sigma_i^\delta \langle \epsilon^i \rangle_- \left(n^i \otimes n^i \right), \tag{9}$$

where ϵ_+ and ϵ_- are the tensile and compressive parts of the strain tensor respectively, ϵ^i are the eigenvalues of the strain tensor, and n^i are their corresponding eigenvectors. This approach partitions the principal strains into compressive and tensile components and then projects them onto their associated principal directions. The sum of these two quantities must equal the total strain. The bracket operators, $\langle \cdot \rangle$, are defined such that:

$$\langle x \rangle_+ := \frac{(x + |x|)}{2} \quad \text{and} \quad \langle x \rangle_- := \frac{(x - |x|)}{2}. \tag{10}$$

Using these conventions for the bracket operator and the strain components, the degraded strain energy density can then be expressed as[35, 36]:

$$\psi_+ = \frac{\lambda_{\text{LLZO}} \langle \text{tr}(\boldsymbol{\epsilon}) \rangle_+^2}{2} + \mu_{\text{LLZO}} \text{tr}(\boldsymbol{\epsilon}_+^2) \quad \text{and} \quad \psi_- = \frac{\lambda_{\text{LLZO}} \langle \text{tr}(\boldsymbol{\epsilon}) \rangle_-^2}{2} + \mu_{\text{LLZO}} \text{tr}(\boldsymbol{\epsilon}_-^2). \tag{11}$$

These strain energy densities can then be used to update the phase-field crack variable. One of the key innovations introduced by Miehe et al. [35] was a strain history field, H. This field represents the largest strain energy associated with tension over the history of the simulation. At each point in the domain, if the present value of the tensile degraded strain energy is greater than the present value of the compressive degraded strain energy and greater than the previous value of H, then H is updated to reflect the new energy value. As H at time $t = n + 1$ is dependent on the displacement field at $t = n$, the variational problem that describes the crack-field evolution is independent of the displacement field at $t = n + 1$ and the two problems may be decoupled and solved in a staggered manner. The phase-field evolution equation for the crack is thus:

$$-\ell^2 \nabla^2 \Phi + \Phi = \frac{2\ell}{G_c} (1 - \Phi) H, \tag{12}$$

where ℓ is the characteristic length scale of the diffuse interface, and G_c represents the classical Griffith fracture energy. This equation is a variational formulation of the linear elastic fracture mechanics, derived by minimizing the free energy associated with generating new crack faces. By leveraging this staggered scheme, we can update the crack field and the displacement fields in sequence via a staggered scheme. We illustrate simple verification and validation cases of our implementation of this fracture model in Appendix B.

2.4. Simulation Setup

To solve the Eqs. (1), (4), and (12), we employed the Mesoscale Multiphysics Phase Field Simulator (MEMPHIS) [38]. This framework discretizes the equations using a central difference scheme. Equations (1), (4), and (12) are solved via successive over-relaxation, the Jacobi method, and the Gauss-Seidel method respectively. These methods iteratively solve the discrete equations until either a prescribed error tolerance is reached or a maximum number of iterations is exceeded.

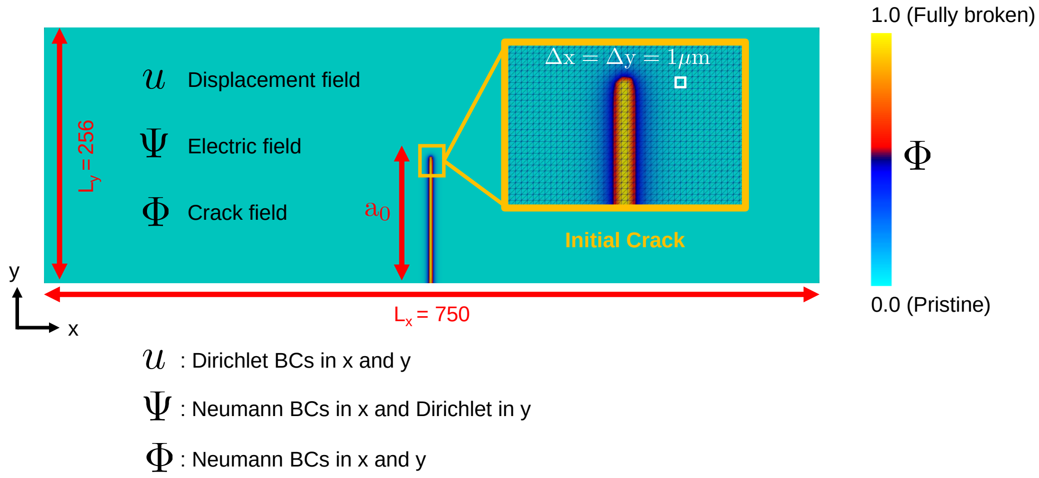

Figure 1: Simulation domain, dimensions, and key features. We solve for three field variables concurrently: displacement field u, electric field Ψ, and crack field Φ. Strains are derived from the displacement field, and stresses are computed from the stresses. Boundary conditions are listed within the geometry of the simulation.

The simulation cell dimensions, mesh size, and crack length scale are kept constant for all simulations. In Fig. 1 we illustrate key fields and boundary equations as well as the dimensions and other key features of the simulation. The dimensions, $\mathrm{L_x}$ and $\mathrm{L_y}$, are set as 768 μm and 256 μm respectively. Selection of $\mathrm{L_x}$ is predicated on allowing enough runway for branching cracks to reach $\mathrm{y} = \mathrm{L_y}$ before reaching $\mathrm{x} = 0$ or $\mathrm{x} = \mathrm{L_x}$. The initial crack length, $\mathrm{a_0}$, refers to the length of either a single initial edge/center crack, or a distribution of lengths for an array of initial cracks. As with any phase-field model, the order parameter is a continuous variable representing a diffuse interface between phases (in this case cracked *vs.* pristine material). The length scale of this diffuse interface, ℓ, is selected to be $2\Delta \mathrm{x}$ [35, 36, 39], or 2 μm.

At the beginning of each simulation, the initial crack geometry is set as either a single crack or a pseudo-random array of many cracks. Single cracks start on the edge of the domain ($\mathrm{x} = \frac{\mathrm{L_x}}{2},\ \mathrm{y} = 0$) and extend to a prescribed length, $\mathrm{a_0}$ ($\mathrm{x} = \frac{\mathrm{L_x}}{2},\ \mathrm{y} = \mathrm{a_0}$). The pseudo-random array of cracks is prescribed starting positions within the simulation domain via a random seed, and then given lengths that satisfy the probability density function (PDF) [40]:

$$P(\mathrm{a}) = \frac{6(\mathrm{a} - \mathrm{a_{min}})(\mathrm{a_{max}} - \mathrm{a})}{(\mathrm{a_{max}} - \mathrm{a_{min}})^3}, \tag{13}$$

where $\mathrm{a_{min}}$ is the minimum prescribed crack length and $\mathrm{a_{max}}$ is the prescribed maximum crack length. The minimum length is set to 1 μm, while the maximum length is set to 20 μm; the number of cracks is selected to meet desired total crack areal density. To capture the effects of both density and spatial distribution of cracks, five conditions are simulated:

1. 1.5 % areal density of cracks
2. 3.0 % areal density of cracks
3. 4.5 % areal density of cracks
4. 4.5 % areal density of cracks, with a 5 μm buffer on top and bottom of the domain
5. 4.5 % areal density of cracks with a 10 μm buffer on top and bottom of the domain.

To generate the cracks for both single and multiple cracks, the strain history field, H, is set to an arbitrarily large number in the area where the crack(s) must be imposed, and Eq. (12) is solved. The electric field is then generated by solving Eq. (1) based on the phase-field crack variable and the applied boundary conditions. The mechanical fields and crack field are then updated in the following scheme:

1. The displacement field is generated from the stresses imposed by the electric field. Strains are computed.
2. The strain energy field is computed and degraded into ψ_+ and ψ_-.
3. ψ_+ is compared to H. If $\psi_+ > H$, $H = \psi_+$.

4. Phase-field crack variable is computed from Eq. (12) from the source term, H.
5. Return to step 1.

This cycle is repeated for ten iterations before progressing to the subsequent step where the electric field is re-calculated to reflect the evolution of the phase-field.

3. Results

We utilized the coupled phase-field model described above to evaluate the maximum electric potential that an LLZO electrolyte can support as a function of crack density. We studied two cases: the simple case when a single edge crack is present, and the more complicated case when the solid electrolyte contains multiple short cracks. The first case is used to gain a fundamental understanding of the unit failure mechanisms at play, while the second case provides us with insights on the operability of a solid electrolyte cell. For both cases, we considered linear sweep voltammetry and constant current conditions. For each condition we evaluated the applied overpotential that LLZO can sustain before crack propagation and short circuit as a function of the crack characteristics (crack length and crack density). In what follows, for clarity's sake, we define failure as any outcome that includes crack propagation, rather than requiring that short circuits evolve.

3.1. Linear Sweep Voltammetry

Linear sweep voltammetry is a method where the potential between the working electrode ($\mathrm{y} = 0$) and the reference electrode ($\mathrm{y} = \mathrm{L_y}$) is swept linearly in time.

3.1.1. Single Edge Crack

In order to probe the electrochemical driving force necessary to induce crack propagation, and eventually short-circuit, we conducted an LSV simulation for single cracks with a ramp rate of 1 mV/sec. These single crack simulations give insight into the resulting mechanics due to overpotential induced stress, as well as the qualitative patterns of initial crack branching. They also provide us with rough benchmarks for permissible applied overpotentials and charging rates based on the largest flaw theory of failure.

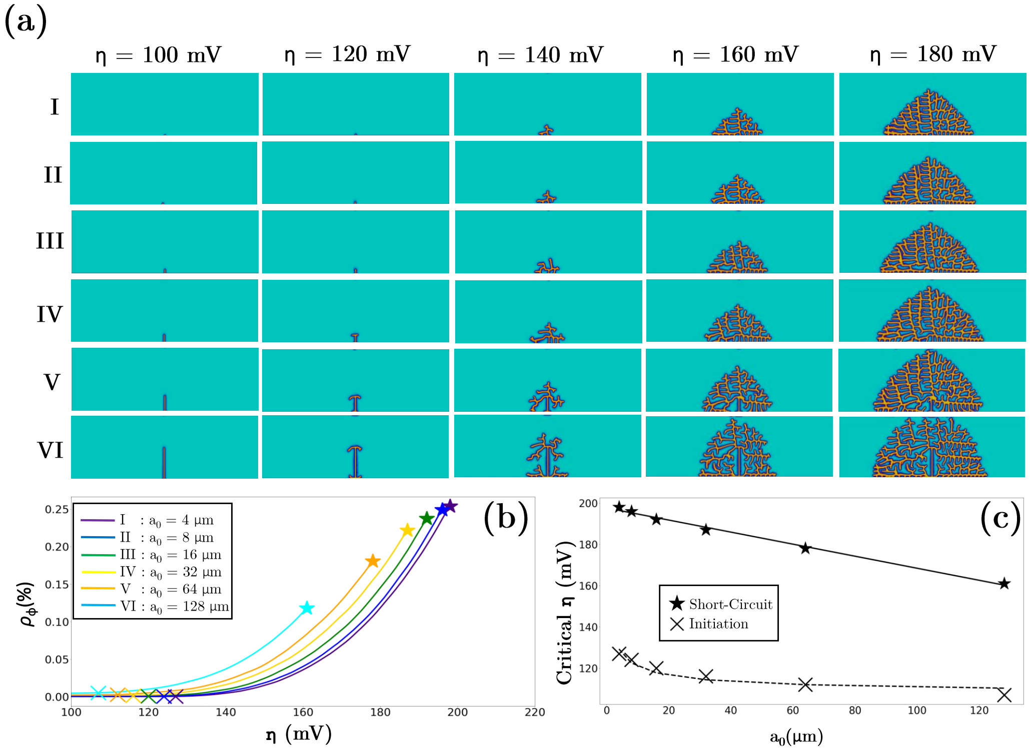

Figure 2: (a) Evolution of crack field for: I. $a_0 = 4\mu$m, II. $a_0 = 8\mu$m, III. $a_0 = 16\mu$m, IV $a_0 = 32\mu$m, V. $a_0 = 64\mu$m, and VI. $a_0 = 128\mu$m. (b) Areal crack density *vs.* applied potential, X symbols represent onset of crack propagation while stars represent short circuit. (c) Critical overpotentials *vs.* initial crack length. Lines represent fits for the two curves.

Figure 2(a) shows the evolution of the crack field for single cracks of initial lengths 4, 8, 16, 32, 64, and 128 μm at several time steps/applied overpotentials. At 100 mV, none of the cracks have advanced, though some additional interface has formed in most cases. At 120 mV, we observe that branches have begun to grow at angles from all initial cracks longer than 32 μm, while shorter cracks remain stationary. By 140 mV, all cracks have begun branching. The branching character of the crack growth matches the results of Ai et al. [37]. The longest crack, by 160 mV, has nearly reached the upper bound of the simulation cell. The final pane of Fig. 2(a) shows that cracks of initial lengths 64 and 128 μm have fully traversed the entire cell domain. The qualitative assessment of these evolutions of the crack field clearly illustrates that the initiation overpotential, η_{init}, and the short-circuit overpotential, η_{sc}, are both inversely dependent on the crack length.

In order to estimate the overpotential at which cracks start to propagate, η_{init}, we define this potential as the potential at the first time step where the order parameter outside of the initial crack interface increases to 1. This time step represents the time at which a previously pristine (uncracked) area element of LLZO has become completely broken. Defining the short-circuit overpotential η_{sc} requires clarification of the fact that the branching crack network can never quite reach $\mathrm{y} = \mathrm{L_y}$ since the upper edge of the domain remains grounded for the duration of the simulation. Thus, we define the short-circuit potential as the potential at which a node's order parameter increases to 1 and is unable to advance any further due to the imposed boundary condition on $\mathrm{y} = \mathrm{L_y}$.

Figure 2(b) shows the growth of crack area calculated as

$$\mathrm{Area} = \int_0^{\mathrm{L_x}} \int_0^{\mathrm{L_y}} \Phi \mathrm{dydx}. \tag{14}$$

Xs are placed where crack propagation begins, while stars are placed at the onset of short circuit. Notably, the linear portions of these crack-growth curves have roughly the same growth rate with respect to the overpotential. The interpretation of this observation is that single cracks grow at a similar rate, regardless of the initial length. In panel (c) of Fig. 2 we quantify the specific scaling with respect to the initial crack length for the initiation and short-circuit overpotentials η_{init} and η_{sc}. From linear elastic fracture mechanics, $K_{\mathrm{I,C}} = g(\sigma_{\mathrm{ff}})\sqrt{\pi \mathrm{a}_c}$, where $g(\sigma_{\mathrm{ff}})$ is some function of the far-field stress and a_c is the critical crack length. However, as the applied loading is electrochemical in nature rather than mechanical, the concept of far-field stress is not applicable; moreover, the loading applied to the crack tip is highly localized. If, instead, we assume that the function g may be expressed as a function of the overpotential η, an inverse square root relationship with respect to a_0 is still to be expected, though with different scaling. Thus, we fit the initiation overpotential η_{init} to an equation of the form:

$$\eta_{\mathrm{init}} = A(\mathrm{a}_0)^{-1/2} + B, \tag{15}$$

where A and B are found to be 46.07 and 106.19 mV respectively with a reasonable quality of fit ($R^2 = 0.92$). In concurrence with the observed similitude of crack growth rates across the range of initial crack lengths surveyed in Fig. 2(b), it is clear that the time to short circuit (and hence the applied overpotential) solely depends on the distance between the initial crack tip and the upper edge of the domain. Consequently, a linear equation is expected to well fit the observed short-circuit overpotential η_{sc} data. Indeed, when this data is fit to a linear form $\eta_{\mathrm{sc}} = Ax + B$, where A is -0.29 mV/$\mu$m and B is 197.60 mV, the fit is extremely high quality ($R^2 > 0.99$), validating the hypothesis that crack growth rate is independent of the initial crack length. Figure 2(c) shows the initiation and short-circuit overpotentials η_{init} and η_{sc} data as well as their corresponding fits.

3.1.2. Multiple Random Cracks

We now turn to the more realistic case where multiple flaws are present within the electrolyte. To establish a more realistic picture of electrochemical fracture in LLZO, 30 samples with pseudo-random crack distributions of varying microstructures are simulated in the same potentiostatic conditions as in the single edge-crack case. Figure 3 shows the evolution of the crack-field variable as a function of applied potential for areal crack densities ranging from 1.5% to 4.5%, without and with a buffer interfacial layer (see Section 2.4). The snapshot selected for each condition is the sample that most closely resembles the ensemble average behavior of that condition. At 100 mV, no samples show any meaningful crack growth. By 120 mV all three of the different densities have begun crack propagation, though to varying degrees; the amount of areal crack density clearly increases with increasing initial crack density. Crack propagation may begin from one or multiple cracks, starting at the charged side of the domain. In our simulations, the load is electrochemical in nature and highly localized to the tips of the initial cracks. Thus, even as a single crack extends, other cracks are not necessarily inhibited. In all cases, crack propagation begins at either larger flaws or clusters of medium-sized flaws that lie close to the charged side of the domain. Flaws farther from the applied potential, in fact, are nonparticipants in crack propagation until the advancing crack front gets near them and their elastic fields may interact. At this point, the cracks will briefly deflect one another and then attract each other and coalesce.

Figure 3(b) shows the variability in the crack-growth behavior as a function of the overpotential for the ensemble averages of each sample; shading spans the standard deviation of the trajectories. Clearly, as crack density increases, terminal crack area increases. This is an intuitive conclusion, as an observer would expect a percolating network of cracks to form more easily

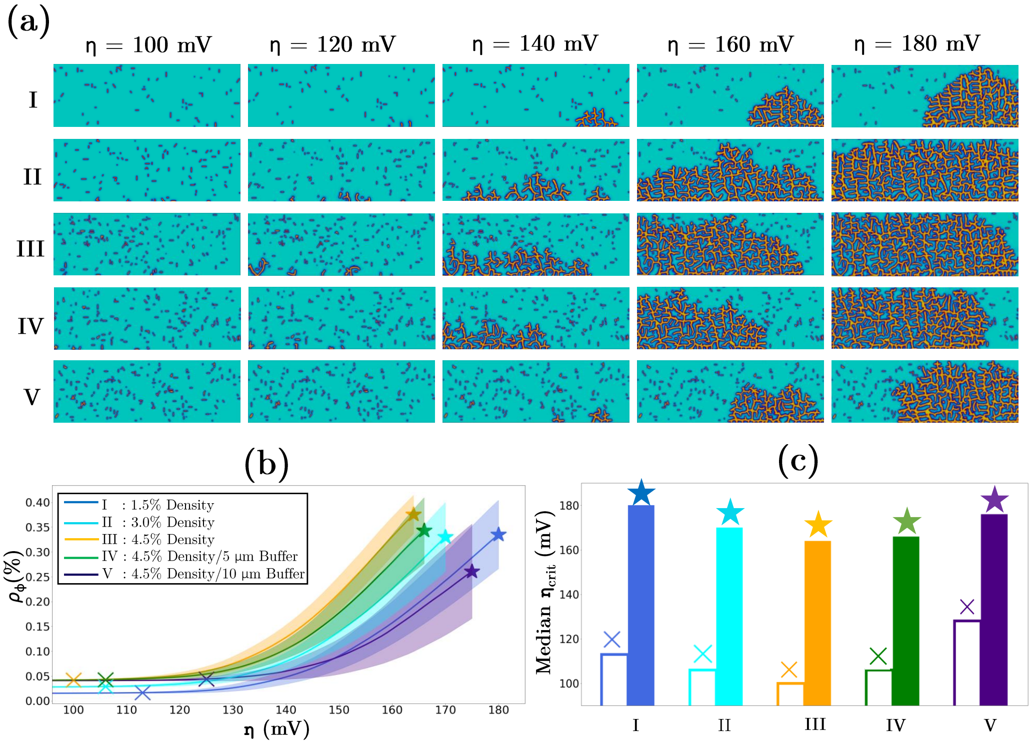

Figure 3: (a) Evolution of the crack field for I. Crack density $\rho_\phi = 1.5\%$, II. Crack density $\rho_\phi = 3.0\%$, III. Crack density $\rho_\phi = 4.5\%$, IV. Crack density $\rho_\phi = 4.5\%$ with a 5 μm buffer, and V. Crack density $\rho_\phi = 4.5\%$, with a 10 μm buffer. (b) Areal crack density *vs.* applied potential, X symbols represent onset of crack propagation while stars represent short circuit. Each line represents the ensemble average of 30 samples for each condition. The shading corresponds to the standard deviation of the crack area values at each time step for each condition. (c) Median critical overpotentials for each condition I through V. X symbols represent onset of crack propagation while star symbols represent short circuit.

with much of the network already in place. This effect also manifests as a decrease in both types of critical overpotentials. The median critical overpotentials of each crack density condition are shown in Fig. 3(c). The observed decay in the medians with respect to increasing crack density demonstrates that the maximum overpotential the material can sustain is sensitive to the extent of initial damage prior to electrochemical loading. Collectively, these results reveals that there is a considerable spread of outcomes for a given density of cracks. To wit, the performance of a given sample of LLZO cannot be deterministically evaluated solely using the density of cracks, as the spatial distribution of cracks of different sizes is a substantial driver of failure. To that end, a statistical framework is employed to evaluate the probability of failure for each condition based on the Weibull model of stochastic failure.

Of the 30 samples for each condition I through V, outliers must first be removed. This pre-screening was only necessary in the case of the 1.5% crack density condition; two samples failed extremely late (crack propagation at 220 and 510 mV respectively), which is several standard deviations higher than the computed median. In these cases, the random seeding did not place any flaws within 10 μm of the edge of the domain, leading to artificially delayed failure.

Adopting a Weibull model of failure allows the probability density function (PDF) of overpotentials to be cast in terms of two parameters, λ and k:

$$\mathrm{PDF}(\eta, \lambda, k) = \frac{k}{\lambda}\left(\frac{\eta}{\lambda}\right)^{k-1} \exp\left[-\left(\frac{\eta}{\lambda}\right)^{k}\right], \tag{16}$$

where λ is a dispersion parameter, and k is the shape parameter determining the shape and sharpness of the peak. From the Weibull distribution follows its cumulative distribution function (CDF):

$$F(\eta, k, \lambda) = 1 - \exp\left[-\left(\frac{\eta}{\lambda}\right)^{k}\right], \tag{17}$$

where F is the probability of failure of the material at or below some value of η. Equation (17) can be rearranged and manipulated to yield a linear fit with a slope of k and a y-intercept of $-k\ln(\lambda)$ such that:

$$\ln\left(-\ln(1 - F(\eta))\right) = k\ln\left(\eta\right) - k\ln\left(\lambda\right), \tag{18}$$

By fitting this equation using linear least squares regression, we found the frequency of failure at various electrochemical loads for our simulations. Table 1 shows the parameters for the Weibull fits as well as the quality of the fits and the median values for short circuit and initiation, while Fig. 4 shows the graphical representation of the fits for both the CDF and the PDF.

Table 1 and Fig. 4 clearly demonstrate that as the areal crack density increases, the overpotentials that LLZO can sustain without crack propagation or short circuit decrease commensurately. Indeed, as seen in the PDF panel of Fig. 4, the median initiation potential from 113 mV to 106 mV to 100 mV as the crack density increases from 1.5 to 3.0 to 4.5 % respectively. Short circuits happen earlier, with the median short-circuit potential decreasing from

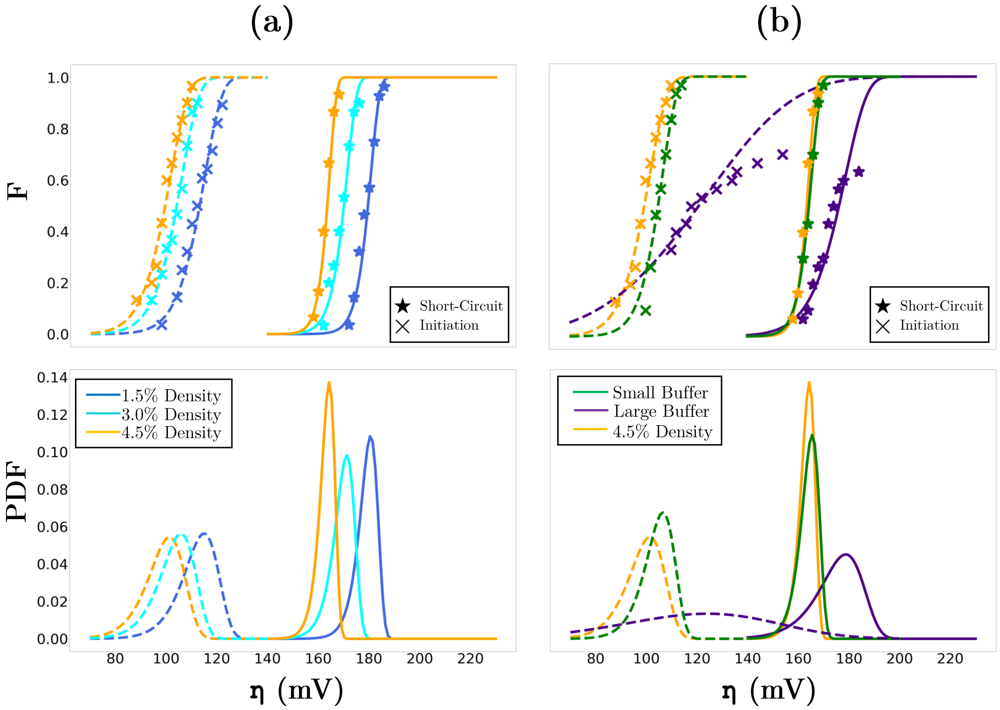

Figure 4: (a) Cumulative distribution function and probability density function comparing crack densities, markers represent experimental data while lines represent Weibull fits. (b) Cumulative distribution function and probability density function comparing buffered and buffer-less samples, markers represent experimental data while lines represent Weibull fits.

180 mV to 170 mV to 164 mV for the same span of crack densities. In other words, the failure distributions shift to favor failure at lower overpotentials as the areal density of cracks is increased.

While a 13% spread in medians over the range of densities is a meaningful difference, it is not substantial. However, the overall behavior of the Weibull distribution will dictate the frequency of failure over a given range of applied potentials, and the total number of failures at each potential is important to consider when gauging the efficacy of a cycling or processing methodology intended to improve the electrochemical durability of the electrolyte material. At 100 mV, for example, roughly 50, 40, and 10 % of samples will fail with a crack areal density of 4.5, 3.0 and 1.5% crack density respectively. While the difference in medians is relatively modest, the spread in the probability

Table 1: Fitted Weibull parameters for each simulated condition and medians for short circuit/initiation.

Condition	$\boldsymbol{\lambda}$	$\boldsymbol{k}$	R^2	$\tilde{\boldsymbol{\eta}}_{\mathrm{init}}$	$\tilde{\boldsymbol{\eta}}_{\mathrm{sc}}$
$\boldsymbol{\rho_\phi = 1.5\%}$	9.09/9.65	12.03/11.78	0.96/0.94	113	180
$\boldsymbol{\rho_\phi = 3.0\%}$	8.58/8.68	12.64/10.75	0.99/0.91	106	170
$\boldsymbol{\rho_\phi = 4.5\%}$	7.55/7.98	11.52/12.16	0.97/0.97	100	164
$\boldsymbol{\rho_\phi = 4.5\%}$**, 5 μm buffer**	7.19/6.98	11.62/12.15	0.95/0.99	106	166
$\boldsymbol{\rho_\phi = 4.5\%}$**, 10 μm buffer**	6.13/5.79	10.74/11.46	0.91/0.87	125	175

density can lead to radically different outcomes on the margins of failure.

The samples with interfacial buffers exhibit a similar increase in the overpotentials that can be supported by the material. Indeed, the 5 μm buffer can support an overpotential that is 6% higher than the baseline, bufferless case, while the 10 μm buffer can support a 25% higher overpotential without crack propagation. Overall density of cracks determines the extent of a percolating crack network (*i.e.* the pathway for short circuit), so the surface density of cracks has little bearing on the short-circuit overpotential, η_{sc}. Thus, as the overall density of cracks is identical in the buffered and buffer-less cases, η_{sc} is very similar between these two cases. The spread for the large buffer is substantially larger, and only a portion of the data could be fit using the Weibull model. While a qualitative assessment of the results show that failure occurs at much higher overpotentials with the large buffer, the precision of the PDF should be evaluated with caution.

3.2. Constant Current

The evolution of a potential field in a battery cell is sensitive to inhomogeneities in the current distribution. Indeed, the current will likely focus in regions of high crack density, where the conductivity is orders of magnitude higher than in the bulk. It is important to evaluate how prevalent this focusing is in damaged samples in order to tailor microstructures that can support greater current densities. Pristine crystals without cracks or defects will evenly distribute the current, leading to smaller overpotentials. Thus, while the buffered samples can support a modestly larger overpotential, the buffer may also distribute the current more evenly through the electrolyte-electrode interface.

We also evaluate the effect of varying the constant currents on a cell with random crack configurations with 4.5% areal crack density with and

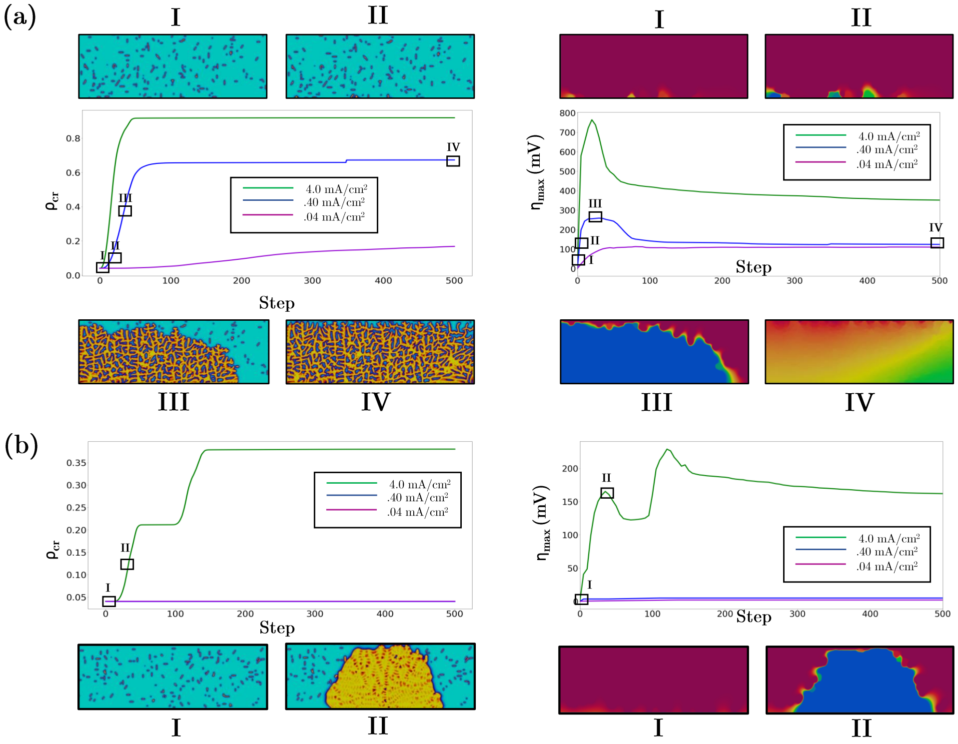

Figure 5: (a) Normalized crack area (left panel) & electric potential (right panel) *vs.* time step with 4.5% areal crack density and no applied buffer. Evolution of the crack field and electric potential are provided as insets for I. $t = 0$, II. The onset of crack propagation, III. The beginning of crack deceleration, minimum overpotential, and IV. The end of the simulation. (b) Normalized crack area (left panel) & electric potential (right panel) *vs.* time step with 4.5% areal crack density and a 5 μm applied buffer. Evolution of the crack field and electric potential are provided as insets for: I. $t = 0$ and II. The end of the simulation. All phase-field insets correspond to samples subjected to 0.40 mA/cm^2.

without a 5 μm pristine buffer. Initially three currents are applied to five samples of each condition: 0.04, 0.4, and 0.40 mA/cm^2. Figure 5 shows how these currents affect the crack field and the maximum overpotential along the interface. The contour plots of the crack and potential fields in both Fig. 5(a) and Fig. 5(b) illustrate the evolution of the system under applied currents of 0.4 mA/cm^2 and 4.0 mA/cm^2 respectively. buffer-less samples exhibited a slow convergence to equilibrium at 0.04 mA/cm^2, but eventually the overpotential exceeds the critical value and crack propagation occurs. At 0.4 mA/cm^2, failure begins in the first several timesteps and progresses steadily to a fully broken equilibrium state. Failure is nearly immediate and complete at 4.0 mA/cm^2. The buffered microstructure is capable of supporting currents of 0.04 and 0.4 mA/cm^2 without generating a critical overpotential anywhere in the domain. In these cases, the initial potential fields show a maximum overpotential of $\sim$ 3-5 mV, well below the critical overpotential for buffered samples. Surface overpotentials remain in this range for the entirety of the simulation and the crack density remains extremely close to the initial value (b.II), showing that the current focusing is essentially eliminated in the buffered sample at these lower current densities. However, a current density of 4.0 mA/cm^2 is sufficient in the buffered sample to induce rapid failure wherein the potential field and crack field propagate rapidly through the domain (b.II).

Figure 5(a) shows the development of these fields for the buffer-less sample. The initial slight variations in the electric field show that there are some regions with a larger overpotentials which corresponds to regions of high crack density near the bottom of the domain (a.I). Clearly, the magnitude of the electric field and therefore the current density is greatest in these regions. This observation illustrates a current focusing mechanism, wherein electrical current (and hence lithium deposition) will preferentially occur near cracks. Roughly, we observe four regimes in our simulation results, the starting configuration (a.I) is followed by a regime in which cracks have begun to grow, coinciding with an electric potential that has dipped precipitously below the critical overpotential for this microstructure (a.II). The maximum overpotential reaches a peak (a.III), coinciding with the cracks traversing the domain. While the cracks continue to grow, the maximum overpotential begins to decrease as the system converges to a stable electric field (a.IV).

Figure 5(b) shows the evolution of the crack and potential fields for a buffered sample at 4.0 mA/cm^2. Buffered samples show ubiquitous success at 0.04 and 0.4 mA/cm^2, but some failures occur at 4.0 mA/cm^2. Of the 5 samples tested, 2 failed and 3 did not fail. The two failures map onto the two precipitous ramps in the average crack density and average voltage curves. While this analysis is sufficient to show that the buffered samples are capable of sustaining higher current than buffer-less samples, it neglects the stochastic elements of failure. To that end, we conducted further Weibull analysis. Figure 6 shows the CDFs and normalized PDFs for samples without and with an interfacial buffer. Comparing the left and right panels in Fig. 6, it is clear that the probability density of failure lies in very different regimes for the two cases. The CDF for the buffer-less case (left panel) spans from

0 to 0.04 mA/cm^2 while the CDF for the buffered case (right panel) spans from 2 to 9 mA/cm^2. At roughly 0.023 mA/cm^2, the buffer-less samples will fail 50% of the time. Failure in buffered samples occurs 50% of the time at 6.0 mA/cm^2, a 200× improvement.

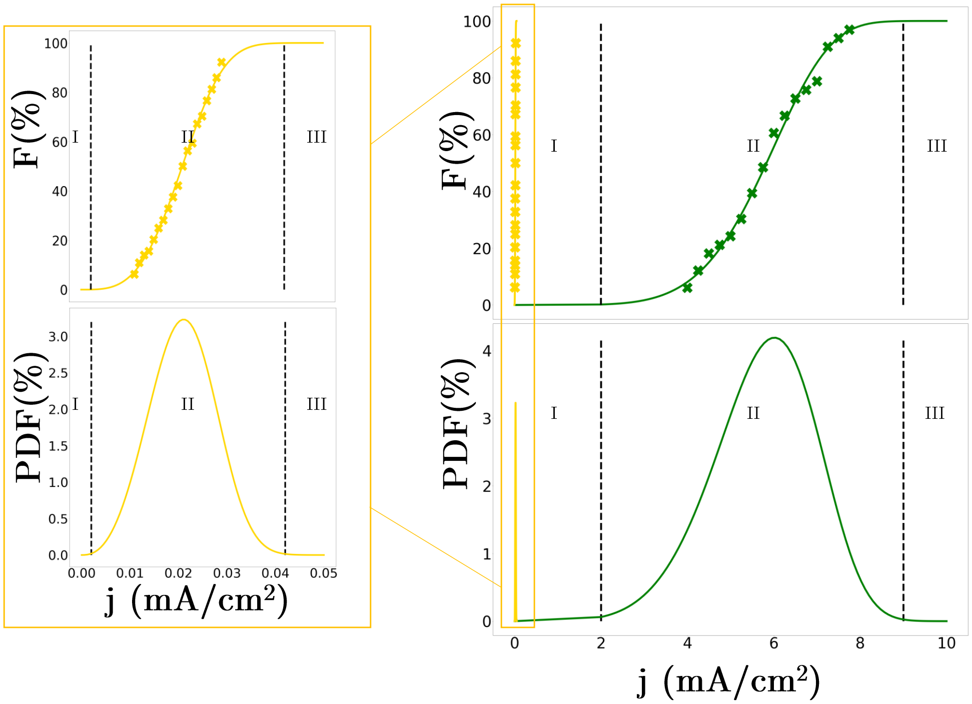

Figure 6: Weibull statistics (CDF and PDF) for samples without and with interfacial buffer. Left inset provides a zoomed in view for the case with no interfacial buffer present. Panel on the right illustrates Weibull statistics for the case with an interfacial buffer present. The three regimes annotated I, II, III correspond to: I. Safe cycling regime, II. Finite cycling regime, and III. Unsafe cycling regime.

4. Discussion

The single crack simulations show that for flaws larger than 4 μm, the critical overpotential required for crack propagation is rather insensitive to the initial crack length. A 30× increase in crack length only leads to a 40% decrease in critical overpotential. By contrast, the critical far-field stress in a simple tension test is predicted to be 80 % lower for a 4 μm crack than a 120 μm crack. As the stresses in the electrochemical loading case are confined around the crack-tip, admissible stress and strain fields must approach zero away from the interface between cracked and uncracked material, leading to the observed difference in scaling. Thus, the key difference between short and long cracks in this context is the magnitude of the electric-field gradient at the crack tip. This explanation introduces a possible mitigation strategy of doping LLZO in order to facilitate electron migration away from crack faces. If the crack faces do not conduct electrons well, the gradients at the crack tip will diminish along with the resultant stresses. Another key feature of the $a_0 - \rho$ curve is that as the fitted curve approaches zero, the critical overpotential required for crack propagation increases substantially. For example, if the largest edge crack were 100 nm, an overpotential of 250 mV could be sustained without any crack growth. It may be possible for battery engineers to screen LLZO samples to estimate the largest flaw and the resultant critical overpotential. Prospective cycling protocols could then be evaluated based on the Butler-Volmer model, or similar, to determine whether the peak projected overpotential exceeds the value determined from an initial screening. Such a framework could be used to improve the lifetimes of LLZO-based cells. Furthermore, battery material engineers could develop strategies for minimizing the size of the largest flaw.

From our analysis, we did not glean information regarding the number of cycles or time to failure at or near the initiation overpotentials. Indeed, while a crack may grow at the initiation potential, it may not traverse the entire thickness of an LLZO film or result in complete inoperability of the material. One should then consider the initiation potential an upper bound for cycling. For example, based on our results, a battery engineer could disregard cycling conditions that exceed an overpotential of 90 mV, as this is likely to lead to short circuit in a finite number of cycles. With *a priori* knowledge of the maximum flaw size, these bounds could be adjusted (*e.g.*, if the largest flaw is 4 μm then the applied overpotential could reach roughly 120 mV and still not incur damage). For applications with shorter life requirements, operating between the initiation and short-circuit overpotential may be a viable option. Thus cycle-life specifications can be determined with knowledge of material flaw-sizes and cycle life can be prescribed based on the overpotentials induced by the necessary cycling protocols.

While a largest-flaw analysis provide approximate benchmarks on operability, a more thorough analysis of the crack distribution is required to extrapolate failure behavior to populations of cells. From our Weibull analysis, it is clear that the density of cracks has a substantial effect on the probability density of failures. While the median critical overpotentials are similar between crack densities, the spread varies substantially. For example, around 115 mV, we project that all samples with a crack density of 4.5 % will fail, while only half of 1.5 % density samples will fail. Understanding the distribution of flaws is germane to predicting the occurrence of failure given an operating potential. The same screening procedure outlined above can be applied from a stochastic framework. In this case, to avoid any crack propagation, cycling should remain at lower overpotentials than the left tail of the initiation PDF. By characterizing the density of cracks and tailoring cycling parameters to keep the overpotential below this tail, a longer life cycle could be achieved (though failure by other mechanisms is of course still possible). If cells are cycled at overpotentials within the span of the short-circuit PDFs, a percentage of them will fail, with the number of failures increasing with increasing potential. This analysis framework informs cycling conditions given some prescribed benchmarks with respect to life cycles and acceptable frequency of failures.

While the experimental determination of crack density can be difficult, a hybrid experimental/analytical approach may be able to determine this key parameter prior to electrochemical operation. Indeed, many experimental studies have been conducted including ring-on-ring and bending tests to evaluate mechanical and fracture properties as well as the statistical characteristics of LLZO's failure behavior in the Weibull sense [14, 41, 42]. To link our modeling framework to such results, our phase-field fracture model could be applied to the loading conditions imposed experimentally with an estimated initial crack density. This initial density would be iteratively revised until computed load-displacement and Weibull curves correspond to those determined experimentally with an acceptable degree of accuracy. Thus, the crack density of a material can be estimated, and the electrically-coupled phase-field model can be applied to project failure curves similar to those reported in this work.

Our results from the voltage sweeps for the buffered samples show an intriguing avenue for improvement of LLZO cells. Indeed, results for the small-buffer case demonstrated a 6 % improvement in median initiation overpotential, while results with a thicker buffer demonstrated a 25 % improvement in median initiation overpotential. Thus, the presence of a pristine buffer has a toughening effect insofar as it limits the exposure of flaws to the full brunt of the electric field. This observation is consistent with the proposed dendrite suppression strategy of Qi et al. [10] using compressive surface stresses. By inducing compressive residual stresses via ion implantation or exchange, the available tensile energy for fracture is reduced, effectively toughening the surface. This method may also heal cracks near the surface, rendering it flawless or near flawless. Importantly, the surface stress-state is sensitive to processing; for instance, Hu et al. [43] showed that rapid cooling can lead to either latent compressive or tensile stresses in the material's surface. Thus, different processing conditions will lead to more flaws and an embrittled surface, or fewer flaws and a toughened surface. Such (residual) stress-state conditions can be accounted for in the present model and used as a way to account for processing conditions.

Our results with a constant current boundary condition reveal a current-focusing mechanism similar to that proposed by Barai et al. [15] with the caveat that the current focusing occurs through regions of high crack density rather than grain boundaries. The large-grained configuration in that study failed at 0.046 mA/cm^2 when the overpotential spiked to 80 mV and short circuited. These observations are congruent with our modeling results for 4.5 % crack density which find that:

- Failure occurs between 0.01 and 0.04 mA/cm^2 (failure is ubiquitous over 0.04 mA/cm^2).
- The critical overpotential for this crack configuration is 100 mV.

Intuitively, we hypothesize that the grain-boundary current focusing and crack-surface current focusing will have synergistic effects. Indeed, it stands to reason that the electric field will be concentrated in cracks that lie along grain boundaries. Probing the interaction between grain boundaries and cracks is a fruitful area for future investigation and is an excellent potential application of this modeling framework. In fact, our model can be thought of as a homogenized, polycrystalline system, or alternatively as an isotropic, single-crystal system. The polycrystalline and/or single-crystal nature of LLZO could be incorporated into our model by assuming anisotropic properties. For instance, in the case of a polycrystal, the model would have heterogeneous distributions of elastic and transport properties to describe the various grains composing the polycrystal. These would be useful extensions of the model due to the ubiquitousness of polycrystalline films [44] and the desirable electrochemical properties of single-crystal LLZO [45].

By contrast to the buffer-less samples' low electrochemical tolerance, the buffered samples fail at currents that would be acceptable for actual battery applications. The current-focusing mechanism is greatly diminished and the resulting lower overpotentials are insufficient to propagate the near-surface cracks. Tuning the interfacial properties of LLZO-Li could facilitate the use of LLZO in battery cells capable of sustaining practical currents and overpotentials. Tuning of this nature comprises any of the methods outlined in the introduction which decrease the electrical conductivity of LLZO. Additionally, the non-participation of cracks further from the interface implicitly shows that methods which increase the flaw tolerance of a near-surface region of the material can decrease the frequency of failures in LLZO at high rates.

5. Conclusion

In this study we use a coupled electrostatics-mechanics phase-field model to evaluate the effects of crack size, crack density, and crack location on the maximum potential and current that LLZO-based cells can support. A few conclusions can be drawn:

1. The initial length of an edge crack decreases the maximum overpotential that can be sustained without crack initiation. Specifically, the critical overpotential increases with the inverse square root of the crack length. This finding demonstrates the cycling limitations from a "largest flaw" perspective.
2. The overpotential at short-circuit scales linearly with the inverse of crack length. This finding demonstrates that the propensity for short circuit depends primarily on the distance between the anode and the cathode. Thicker electrolyte films should fail later than thinner ones.
3. Systems with multiple cracks fail more at higher density than lower density. This manifests strongly at the tails of the cumulative distribution functions. An overpotential that is completely safe for operation in LLZO with 1.5% areal crack density carries a comparatively high probability of failure at 4.5% areal density.
4. When constant currents are applied, larger overpotentials arise inside the electrolyte domain, specifically in regions where there are near-surface cracks. This current-focusing mechanism leads to rapid failure at very low currents (10 - 40 mA/cm^2).

5. Samples with a pristine, interfacial buffer are able to sustain greater potentials than the base material at equivalent crack density. The buffered material also exhibits lower potentials in response to applied constant currents. These two effects compound to allow a two order of magnitude improvement in the current that the buffered material can support.

These observations demonstrate that a careful evaluation of crack density is important to battery engineers for evaluating safe cycling parameters for LLZO-based cells. Even the simpler largest flaw model may be sufficient to set rough operability benchmarks with safety factors included. We have also established that a Weibull-type model describes the relationship between applied potential,current and failure. This is critical as it characterizes the stochastic nature of failure in larger populations of cells, allowing for predictions of failure in terms of proportion rather than a simple binary pass/fail for prescribed potentials or currents. By exploring the benefit of a flawless buffer of crystal, we demonstrate several possible mitigation strategies which guide future modeling and experimental studies of this material and could lead to the enabling of LLZO as a commercially viable material.

CRediT authorship contribution statement

S. Monismith: Conceptualization, Methodology/Study design, Software, Validation, Formal analysis, Investigation, Data curation, Writing – original draft, Writing – review and editing, Visualization. **J. Qu:** Conceptualization, Methodology/Study design, Investigation, Resources, Writing – original draft, Writing – review and editing, Supervision, Project administration, Funding acquisition. **R. Dingreville:** Conceptualization, Methodology/Study design, Software, Validation, Formal analysis, Investigation, Resources, Writing – original draft, Writing – review and editing, Visualization, Supervision.

Declaration of competing interest

The authors declare that they have no known competing financial interests or personal relationships that could have appeared to influence the work reported in this paper.

Acknowledgements

The phase-field framework is developed and supported by the Center for Integrated Nanotechnologies, an Office of Science User Facility operated for the U.S. Department of Energy. This work was performed, in part, at the Center for Integrated Nanotechnologies, an Office of Science User Facility operated for the U.S. Department of Energy. The authors also acknowledge the Tufts University High Performance Compute Cluster (https://it.tufts.edu/high-performance-computing) which was utilized for a portion of the research reported in this paper. This article has been authored by an employee of National Technology & Engineering Solutions of Sandia, LLC under Contract No. DE-NA0003525 with the U.S. Department of Energy (DOE). The employee owns all right, title and interest in and to the article and is solely responsible for its contents. The United States Government retains and the publisher, by accepting the article for publication, acknowledges that the United States Government retains a non-exclusive, paid-up, irrevocable, world-wide license to publish or reproduce the published form of this article or allow others to do so, for United States Government purposes. The DOE will provide public access to these results of federally sponsored research in accordance with the DOE Public Access Plan https://www.energy.gov/downloads/doe-public-access-plan.

Appendix A. Nomenclature

Table A.1: Glossary of fields and key terms

Φ	Crack field
Ψ	Electric potential
u	Displacement field
σ^{elec}	Total electrical conductivity
$\mathrm{h}(\Phi)$	Interpolation function between cracked/uncracked phase
η	Overpotential, deviation from equilibrium
$\mathrm{j}_{\mathrm{applied}}$	Applied current
σ^0	Stress due to electrolyte mechanical constraint
σ^η	Stress that arises from applied overpotential
ϵ_+	Tensile portion of strain tensor
ϵ_-	Compressive portion of strain tensor
$\mathbb{C}$	Elastic stiffness tensor
$\mu_{\mathrm{LLZO}}, \lambda_{\mathrm{LLZO}}$	Lamé elastic constants
ψ_+, ψ_-	Strain energy density from tension/compression
H	Strain history field
ℓ	Characteristic length scale for fracture
G_c	Griffith fracture energy
$\mathrm{L_x}, \mathrm{L_y}$	Dimension of computational domain in x and y
$\eta_{\mathrm{init}}, \eta_{\mathrm{sc}}$	Crack initiation/short-circuit overpotentials
ρ_ϕ	Crack density
PDF	Probability density function
CDF	Cumulative distribution function
k, λ	Weibull distribution parameters

Appendix B. Static Fracture Simulations

We implemented, verified, and tested the phase-field fracture model presented in Miehe et al. [35] and Ambati et al. [36]. Figure B.1 shows the results of our implementation for LLZO subjected under simple shear (top panel) and simple tension (middle panel). The bottom panel illustrates the stress-strain behavior during the evolution of the crack.

Figure B.1: Simulation results for simple shear (top) and simple tension (bottom).

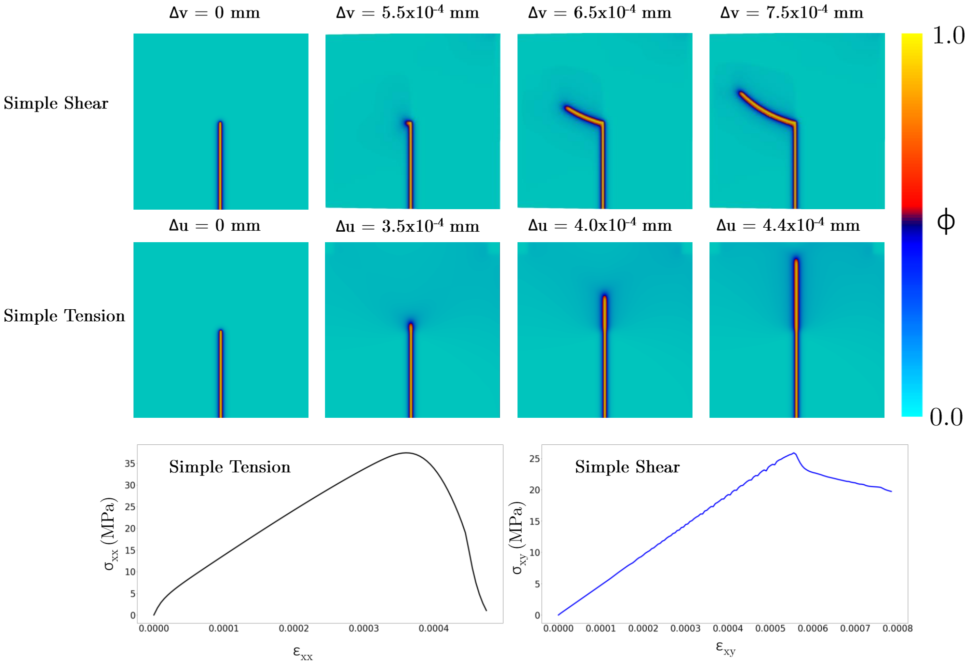

References

[1] J. L. Allen, J. Wolfenstine, E. Rangasamy, J. Sakamoto, Effect of substitution (Ta, Al, Ga) on the conductivity of $Li_7La_3Zr_2O_{12}$, Journal of Power Sources 206 (2012) 315–319. doi:10.1016/j.jpowsour.2012.01.131.

[2] T. Thompson, S. Yu, L. Williams, R. D. Schmidt, R. Garcia-Mendez, J. Wolfenstine, J. L. Allen, E. Kioupakis, D. J. Siegel, J. Sakamoto, Electrochemical window of the Li-ion solid electrolyte $Li_7La_3Zr_2O_{12}$, ACS Energy Letters 2 (2017) 462–468. doi:10.1021/acsenergylett.6b00593.

[3] C. Monroe, J. Newman, The impact of elastic deformation on deposition kinetics at lithium/polymer interfaces, Journal of The Electrochemical Society 152 (2005) A396. doi:10.1149/1.1850854.

[4] Y. Kim, H. Jo, J. L. Allen, H. Choe, J. Wolfenstine, J. Sakamoto, The effect of relative density on the mechanical properties of hot-pressed cubic $Li_7La_3Zr_2O_{12}$, Journal of the American Ceramic Society 99 (2016) 1367–1374. doi:10.1111/jace.14084.

[5] Y. Kim, H. Jo, J. L. Allen, H. Choe, J. Wolfenstine, J. Sakamoto, The effect of relative density on the mechanical properties of hot-pressed cubic $Li_7La_3Zr_2O_{12}$, Journal of the American Ceramic Society 99 (2016) 1367–1374. doi:10.1111/jace.14084.

[6] J. Wolfenstine, J. L. Allen, J. Sakamoto, D. J. Siegel, H. Choe, Mechanical behavior of Li-ion-conducting crystalline oxide-based solid electrolytes: a brief review, Ionics 24 (2018) 1271–1276. doi:10.1007/s11581-017-2314-4.

[7] A.-N. Wang, J. F. Nonemacher, G. Yan, M. Finsterbusch, J. Malzbender, M. Krüger, Mechanical properties of the solid electrolyte al-substituted $Li_7La_3Zr_2O_{12}$ (LLZO) by utilizing micro-pillar indentation splitting test, Journal of the European Ceramic Society 38 (2018) 3201–3209. doi:10.1016/j.jeurceramsoc.2018.02.032.

[8] L. Cheng, W. Chen, M. Kunz, K. Persson, N. Tamura, G. Chen, M. Doeff, Effect of surface microstructure on electrochemical performance of

garnet solid electrolytes, ACS Applied Materials and Interfaces 7 (2015) 2073–2081. doi:10.1021/am508111r.

[9] L. Porz, T. Swamy, B. W. Sheldon, D. Rettenwander, T. Frömling, H. L. Thaman, S. Berendts, R. Uecker, W. C. Carter, Y. M. Chiang, Mechanism of lithium metal penetration through inorganic solid electrolytes, Advanced Energy Materials 7 (2017) 1–12. doi:10.1002/aenm.201701003.

[10] Y. Qi, C. Ban, S. J. Harris, A new general paradigm for understanding and preventing Li metal penetration through solid electrolytes, Joule 4 (2020) 2599–2608. doi:10.1016/j.joule.2020.10.009.

[11] R. Raj, J. Wolfenstine, Current limit diagrams for dendrite formation in solid-state electrolytes for Li-ion batteries, Journal of Power Sources 343 (2017) 119–126. doi:10.1016/j.jpowsour.2017.01.037.

[12] T. Swamy, R. Park, B. W. Sheldon, D. Rettenwander, L. Porz, S. Berendts, R. Uecker, W. C. Carter, Y.-M. Chiang, Lithium metal penetration induced by electrodeposition through solid electrolytes: Example in single-crystal $Li_7La_3Zr_2O_{12}$ garnet, Journal of The Electrochemical Society 165 (2018) A3648–A3655. doi:10.1149/2.1391814jes. arXiv:1808.02105.

[13] T. Krauskopf, B. Mogwitz, H. Hartmann, D. K. Singh, W. G. Zeier, J. Janek, The fast charge transfer kinetics of the lithium metal anode on the garnet-type solid electrolyte $Li_{6.25}Al_{0.25}La_3Zr_2O_{12}$, Advanced Energy Materials 10 (2020). doi:10.1002/aenm.202000945.

[14] J. Wolfenstine, H. Jo, Y. H. Cho, I. N. David, P. Askeland, E. D. Case, H. Kim, H. Choe, J. Sakamoto, A preliminary investigation of fracture toughness of $Li_7La_3Zr_2O_{12}$ and its comparison to other solid Li-ionconductors, Materials Letters 96 (2013) 117–120. doi:10.1016/j.matlet.2013.01.021.

[15] P. Barai, A. T. Ngo, B. Narayanan, K. Higa, L. A. Curtiss, V. Srinivasan, The role of local inhomogeneities on dendrite growth in LLZO-based solid electrolytes, Journal of the Electrochemical Society 167 (2020) 100537. doi:10.1149/1945-7111/ab9b08.

[16] S. Monismith, J. Qu, R. Dingreville, Grain-boundary fracture mechanisms in $Li_7La_3Zr_2O_{12}$ (LLZO) solid electrolytes : When phase transformation acts as a temperature-dependent toughening mechanism, Journal of the Mechanics and Physics of Solids 160 (2022) 104791. doi:10.1016/j.jmps.2022.104791.

[17] X. Li, L. Cong, S. Ma, S. Shi, Y. Li, S. Li, S. Chen, C. Zheng, L. Sun, Y. Liu, H. Xie, Low resistance and high stable solid–liquid electrolyte interphases enable high-voltage solid-state lithium metal batteries, Advanced Functional Materials 31 (2021) 2010611. doi:https://doi.org/10.1002/adfm.202010611.

[18] S. Yan, S. Abouali, C. H. Yim, J. Zhou, J. Wang, E. A. Baranova, A. Weck, V. Thangadurai, A. Merati, Y. Abu-Lebdeh, Revealing the Role of Liquid Electrolytes in Cycling of Garnet-Based Solid-State Lithium-Metal Batteries, Journal of Physical Chemistry C 126 (2022) 14027–14035. doi:10.1021/acs.jpcc.2c02074.

[19] A. M. Bates, Y. Preger, L. Torres-Castro, K. L. Harrison, S. J. Harris, J. Hewson, Are solid-state batteries safer than lithium-ion batteries?, Joule 6 (2022) 742–755. doi:10.1016/j.joule.2022.02.007.

[20] C. Yuan, X. Gao, Y. Jia, W. Zhang, Q. Wu, J. Xu, Coupled crack propagation and dendrite growth in solid electrolyte of all-solid-state battery, Nano Energy 86 (2021) 106057. doi:10.1016/j.nanoen.2021.106057.

[21] C. Lee, S. Y. Han, J. A. Lewis, P. P. Shetty, D. Yeh, Y. Liu, E. Klein, H. W. Lee, M. T. McDowell, Stack pressure measurements to probe the evolution of the lithium-solid-state electrolyte interface, ACS Energy Letters 6 (2021) 3261–3269. doi:10.1021/acsenergylett.1c01395.

[22] R. A. Ahmed, N. Ebechidi, I. Reisya, K. Orisekeh, A. Huda, A. Bello, O. K. Oyewole, W. O. Soboyejo, Pressure-induced interfacial contacts and the deformation in all solid-state Li-ion batteries, Journal of Power Sources 521 (2022) 230939. URL: https://doi.org/10.1016/j.jpowsour.2021.230939. doi:10.1016/j.jpowsour.2021.230939.

[23] S. Yu, D. J. Siegel, Atomic scale simulations of the solid electrolyte $Li_7La_3Zr_2O_{12}$, Transition Metal Oxides for Electrochemical Energy Storage (2022) 375–391. doi:10.1002/9783527817252.ch15.

[24] P. Barai, K. Higa, A. T. Ngo, L. A. Curtiss, V. Srinivasan, Mechanical stress induced current focusing and fracture in grain boundaries, Journal of The Electrochemical Society 166 (2019) A1752–A1762. doi:10.1149/2.0321910jes.

[25] L. Chen, H. W. Zhang, L. Y. Liang, Z. Liu, Y. Qi, P. Lu, J. Chen, L. Q. Chen, Modulation of dendritic patterns during electrodeposition: A nonlinear phase-field model, Journal of Power Sources 300 (2015) 376–385. doi:10.1016/j.jpowsour.2015.09.055.

[26] V. Yurkiv, T. Foroozan, A. Ramasubramanian, R. Shahbazian-Yassar, F. Mashayek, Phase-field modeling of solid electrolyte interface (SEI) influence on Li dendritic behavior, Electrochimica Acta 265 (2018) 609–619. doi:10.1016/j.electacta.2018.01.212.

[27] C. D. Fincher, D. Ojeda, Y. Zhang, G. M. Pharr, M. Pharr, Mechanical properties of metallic lithium: from nano to bulk scales, Acta Materialia 186 (2020) 215–222. doi:10.1016/j.actamat.2019.12.036.

[28] L. L. Dienemann, A. Saigal, M. A. Zimmerman, Creep and anisotropy of free-standing lithium metal foils in an industrial dry room, Journal of Electrochemical Energy Conversion and Storage 18 (2021). doi:10.1115/1.4052043, 040908.

[29] L. Gao, Z. Guo, Phase-field simulation of Li dendrites with multiple parameters influence, Computational Materials Science 183 (2020). doi:10.1016/j.commatsci.2020.109919.

[30] Z. Hong, V. Viswanathan, Phase-field simulations of lithium dendrite growth with open-source software, ACS Energy Letters 3 (2018) 1737–1743. doi:10.1021/acsenergylett.8b01009. arXiv:1805.03256.

[31] Y. Ren, Y. Zhou, Y. Cao, Inhibit of lithium dendrite growth in solid composite electrolyte by phase-field modeling, The Journal of Physical Chemistry C 124 (2020) 12195–12204. doi:10.1021/acs.jpcc.0c01116.

[32] H. K. Tian, Z. Liu, Y. Ji, L. Q. Chen, Y. Qi, Interfacial electronic properties dictate Li dendrite growth in solid electrolytes, Chemistry of Materials 31 (2019) 7351–7359. doi:10.1021/acs.chemmater.9b01967.

[33] H.-K. Tian, B. Xu, Y. Qi, Computational study of lithium nucleation tendency in $Li_7La_3Zr_2O_{12}$ (LLZO) and rational design of interlayer materials to prevent lithium dendrites, Journal of Power Sources 392 (2018) 79–86. doi:10.1016/j.jpowsour.2018.04.098.

[34] C. Yuan, W. Lu, J. Xu, Unlocking the electrochemical–mechanical coupling behaviors of dendrite growth and crack propagation in all-solid-state batteries, Advanced Energy Materials 11 (2021) 2101807. doi:10.1002/aenm.202101807.

[35] C. Miehe, M. Hofacker, F. Welschinger, A phase field model for rate-independent crack propagation: Robust algorithmic implementation based on operator splits, Computer Methods in Applied Mechanics and Engineering 199 (2010) 2765–2778. doi:10.1016/j.cma.2010.04.011.

[36] M. Ambati, T. Gerasimov, L. De Lorenzis, A review on phase-field models of brittle fracture and a new fast hybrid formulation, Computational Mechanics 55 (2015) 383–405. doi:10.1007/s00466-014-1109-y.

[37] W. Ai, B. Wu, E. Martínez-Pañeda, A coupled phase field formulation for modelling fatigue cracking in lithium-ion battery electrode particles, Journal of Power Sources 544 (2022) 231805. doi:10.1016/j.jpowsour.2022.231805.

[38] J. A. Stewart, R. Dingreville, Microstructure morphology and concentration modulation of nanocomposite thin-films during simulated physical vapor deposition, Acta Materialia 188 (2020) 181–191. doi:10.1016/j.actamat.2020.02.011.

[39] S. Natarajan, R. K. Annabattula, et al., A FEniCS implementation of the phase field method for quasi-static brittle fracture, Frontiers of Structural and Civil Engineering 13 (2019) 380–396. doi:10.1007/s11709-018-0471-9.

[40] R. F. Cook, F. W. DelRio, Material flaw populations and component strength distributions in the context of the Weibull function, Experimental Mechanics 59 (2019) 279–293. doi:10.1007/s11340-018-0423-2.

[41] G. Yan, J. F. Nonemacher, H. Zheng, M. Finsterbusch, J. Malzbender, M. Krüger, An investigation on strength distribution, subcritical

crack growth and lifetime of the lithium-ion conductor $Li_7La_3Zr_2O_{12}$, Journal of Materials Science 54 (2019) 5671–5681. doi:10.1007/s10853-018-03251-4.

[42] J. F. Nonemacher, Y. Arinicheva, G. Yan, M. Finsterbusch, M. Krüger, J. Malzbender, Fracture toughness of single grains and polycrystalline $Li_7La_3Zr_2O_{12}$ electrolyte material based on a pillar splitting method, Journal of the European Ceramic Society 40 (2020) 3057–3064. doi:10.1016/j.jeurceramsoc.2020.03.028.

[43] J. Hu, Z. Sun, Y. Gao, P. Li, Y. Wu, S. Chen, R. Wang, N. Li, W. Yang, Y. Shen, S.-H. Bo, 3D stress mapping reveals the origin of lithium-deposition heterogeneity in solid-state lithium-metal batteries, Cell Reports Physical Science 3 (2022) 100938. doi:10.1016/j.xcrp.2022.100938.

[44] C. Zheng, Y. Lu, J. Su, Z. Song, T. Xiu, J. Jin, M. E. Badding, Z. Wen, Grain boundary engineering enabled high-performance garnet-type electrolyte for lithium dendrite free lithium metal batteries, Small Methods 6 (2022) 2200667. doi:10.1002/smtd.202200667.

[45] K. Kataoka, Oxide single crystals with high lithium-ion conductivity as solid electrolytes for all-solid-state lithium secondary battery applications, Journal of the Ceramic Society of Japan 128 (2020) 7–18. doi:10.2109/jcersj2.19094.